Progress In Electromagnetics Research M, Vol. 85, 29–38, 2019

Improvement of Resolution of Liquid Refractive Index Measurement Using Metallic Grating

Taikei Suyama[1, *], Zhaoxia Qian[2], Fenghui Shi[1], Hiroki Enomoto[1], and Akira Matsushima[3]

Abstract—The excitation of surface plasmon on a metallic grating can be observed by varying the polar angle, accompanied by the absorption of incident light. The absorption occurs at a resonance angle which is sensitive to the refractive index of the liquid coated on the surface of the grating. As a result, an application in index sensing is developed. However, the sensitivity by varying the polar angle is almost at the same level as a conventional prism couple-based sensor through angular detection. In our new setup, we propose two methods to improve the sensitivity to refractive index change using an index sensor. Our first method is a slight modification of the conventional setup by varying the azimuth angle instead of the polar angle. Absorption of the incident is also observed while scanning the azimuth angle. The second method is to utilize phase detection to realize high resolution in finding the refractive index of liquids. In the phase detection, a good linearity is observed in the experimental results, with a resolution 10 times higher than that of a conventional setup.

1. INTRODUCTION

A metallic grating has a property known as resonance absorption: partial or total absorption of incident light energy occurs at a specific angle of incidence resonance, which is called surface plasmon resonance [1–4]. Surface plasmon is a collective longitudinal vibration of free electrons on the metal surface. Since the surface plasmon resonance absorption phenomenon in the metallic grating is strongly influenced by the refractive index of the medium on the surface of the metallic grating, it is expected that the metallic grating is used for measuring the liquid refractive index [5–8].

A refractive index sensor utilizing surface plasmon resonance absorption is called a surface plasmon resonance sensor (SPR sensor). Although SPR sensors are applied in various fields such as DNA profiling and immunoassay [9–11], improvement of resolution is required to perform measurement with higher precision. Although a plasmon index sensor with a prism has been examined by many researchers in detail, few works with a metallic grating have been reported. We have examined the possibility of employing the plasmon resonance absorption on a metallic grating as an index sensor [12, 13]. As a result, an application in index sensing is developed. However, the sensitivity by the polar angle is less than 120°/RIU, which is almost at the same level as a conventional prism couple-based sensor through angular detection [14, 15]. In order to improve the resolution of liquid refractive index measurement using a metallic grating, we have successfully built a high-resolution refractive index sensor by performing azimuth angle and phase measurement in addition to measurement of diffraction efficiency of reflected light.

Received 3 June 2019, Accepted 18 August 2019, Scheduled 9 September 2019

* Corresponding author: Taikei Suyama (suyama@akashi.ac.jp).

[1] National Institute of Technology, Akashi College, 679-3 Nishioka, Uozumi-cho, Akashi, Hyogo 674-8501, Japan. [2] Expedia Group, 333 108th Avenue NE, Bellevue, WA 98004, USA. [3] Faculty of Advanced Science and Technology, Kumamoto University, 2-39-1 Kurokami, Kumamoto 860-8555, Japan.

2. METALLIC GRATING, INCIDENT LIGHT AND DIFFRACTED FIELDS

This section is a brief introduction of the metallic grating, incident light, and diffracted fields. In this paper, a time factor $\exp(-i\omega t)$ is suppressed.

2.1. Metallic Grating and Incident Light

Figure 1 shows the schematic representation of diffraction by a layered grating made of a metal and having an over-coating thin oxide film. The grating is uniform in the Y direction and periodic in the X direction. The surface profiles are given by

$$S_1{:}z_1 \;=\; \eta_1(x) = h\sin\left(\frac{2\pi x}{d}\right) \tag{1}$$

$$S_2{:}z_2 \;=\; \eta_2(x) = h\sin\left(\frac{2\pi x}{d}\right) - e \tag{2}$$

where h, d, and e are the amplitude (half depth) of the surface modulation, the period, and the thickness of the coating. Note that the small letters (x, y, z) denote a point on the surfaces.

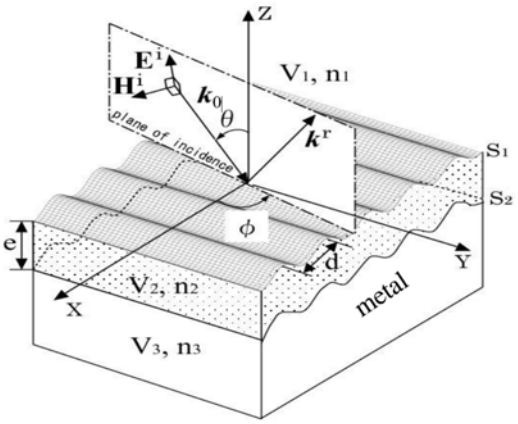

Figure 1. Schematic representation of diffraction by a metallic grating.

We assume that the volume regions V_1, V_2, and V_3 defined by

$$V_1 : Z > \eta_1(X) \quad \text{(free space)} \tag{3}$$

$$V_2 : \eta_2(X) < Z < \eta_1(X) \quad \text{(oxide film)} \tag{4}$$

$$V_3 : Z < \eta_2(X) \quad \text{(metal)} \tag{5}$$

are filled with a dielectric (with a positive refractive index n_1), a oxide film (with a positive refractive index n_2), and metal (with a complex n_3), respectively. Note that (X, Y, Z) denotes the coordinates of a point in these regions. A convention $P = (X, Y, Z)$ will be used as well. The electric and magnetic fields of an incident light is given by

$$\mathbf{E}^i(P) \;=\; \mathbf{e}_0 \exp(i\mathbf{k}_0 \cdot \mathbf{P}) \tag{6}$$

$$\mathbf{H}^i(P) \;=\; \mathbf{h}_0 \exp(i\mathbf{k}_0 \cdot \mathbf{P}) \tag{7}$$

with

$$\mathbf{h}_0 = (\omega\mu)^{-1}\,\mathbf{k}_0 \times \mathbf{e}_0 \tag{8}$$

Here, $\mathbf{e}_0$ is the electric-field amplitude, and $\mathbf{k}_0$ is the incident wave vector

$$\mathbf{k}_0 = (\alpha, \beta, -\gamma) \tag{9}$$

with $\alpha = k_0 \sin\theta\cos\phi$, $\beta = k_0 \sin\theta\sin\phi$, $\gamma = k_0\cos\theta$ and $k_0 = 2\pi/\lambda$. As shown in Fig. 1, θ is the polar angle between the Z-axis and incident wave-vector, ϕ the azimuth angle between the X-axis and plane of incidence, and λ the wavelength in vacuum.

Let us decompose the amplitude of the incident light into a TE- and a TM-component, where TE (or TM) means the absence of the Z-component in the relevant electric (or magnetic) field. To do this, we first define two unit vectors that span a plane orthogonal to $\mathbf{k}_0$

$$\mathbf{e}^{\mathrm{TE}} = (\sin\phi, -\cos\phi, 0) \tag{10}$$

$$\mathbf{e}^{\mathrm{TM}} = (\cos\theta\cos\phi, \cos\theta\sin\phi, \sin\theta) \tag{11}$$

Apparently, $\mathbf{e}^{\mathrm{TE}}$ has no Z-component. The fact that the magnetic amplitude accompanying $\mathbf{e}^{\mathrm{TM}}$ cannot have any Z-component can be seen by direct manipulation. In addition, they are perpendicular to each other, and both of them make a right angle with $\mathbf{k}_0$. Hence, they are unit vectors in the direction of the TE- and TM-components in the sense above. The amplitude $\mathbf{e}_0$ is decomposed as

$$\mathbf{e}_0 = \cos\delta\cdot\mathbf{e}^{\mathrm{TE}} + \sin\delta\cdot\mathbf{e}^{\mathrm{TM}} \tag{12}$$

where δ is the angle between $\mathbf{e}^{\mathrm{TE}}$ and $\mathbf{e}_0$ and is termed as a polarization angle. Thus, the incident light is specified by the wavelength λ, the polar and azimuth angles θ and ϕ, and the polarization angle δ.

2.2. The Diffracted Fields

Because the diffracted fields have both TE- and TM-components, we need TE and TM vector modal functions to construct solutions. The modal functions are derived from the Floquet modes and are defined by

$$\boldsymbol{\varphi}_{qm}^{\mathrm{TE}}(P) = \mathbf{e}_{qm}^{\mathrm{TE}} \exp(i\mathbf{k}_{qm}\cdot\mathbf{P}) \tag{13}$$

$$\boldsymbol{\varphi}_{qm}^{\mathrm{TM}}(P) = \mathbf{e}_{qm}^{\mathrm{TM}} \exp(i\mathbf{k}_{qm}\cdot\mathbf{P}) \tag{14}$$

for $m = 0, \pm1, \pm2, \ldots$ ($\mathbf{P}\in V_q$; $q = 1, 2, 3$). Here,

$$\mathbf{e}_{qm}^{\mathrm{TE}} = \frac{\mathbf{k}_{qm}\times\mathbf{i}_z}{|\mathbf{k}_{qm}\times\mathbf{i}_z|}, \quad \mathbf{e}_0^{\mathrm{TM}} = \frac{\mathbf{e}_{qm}^{\mathrm{TE}}\times\mathbf{k}_{qm}}{|\mathbf{e}_{qm}^{\mathrm{TE}}\times\mathbf{k}_{qm}|} \tag{15}$$

and

$$\mathbf{k}_{1m} = (\alpha_m, \beta, -\gamma_{1m}) \tag{16}$$

$$\mathbf{k}_{2m} = (\alpha_m, \beta, \mp\gamma_{2m}) \tag{17}$$

$$\mathbf{k}_{3m} = (\alpha_m, \beta, -\gamma_{3m}) \tag{18}$$

with

$$\alpha_m = \alpha + \frac{2m\pi}{d} \tag{19}$$

$$\gamma_{qm} = \sqrt{(n_q\mathbf{k}_0)^2 - (\alpha_m^2 + \beta^2)} \tag{20}$$

Note that the modal functions given in Eqs. (13) and (14) are employed in constructing diffracted electric fields. For magnetic fields, we define alternative sets of modal functions:

$$\boldsymbol{\psi}_{qm}^{j} = \frac{1}{\omega\mu_0}\mathbf{k}_{qm}\times\boldsymbol{\varphi}_{qm}^{j} \ (j = \mathrm{TE}, \mathrm{TM}) \tag{21}$$

which are obtained from Eqs. (13) and (14) through Maxwell's equations.

Approximate solutions in V_1 are finite sums of up-going modal functions with unknown modal coefficients. Likewise, the solutions in V_3 are linear combinations of down-going modal functions, whereas in V_2, the solutions must have oscillating modal functions. All the solutions should consist of TE- and TM-components except the planar mounting case. The approximate solutions in each region, hence, can be expressed as:

$$\begin{pmatrix}\mathbf{E}_{qN}^{d}\\ \mathbf{H}_{qN}^{d}\end{pmatrix}(P) = \sum_{m=-N}^{N} U_{qm}^{\mathrm{TE}}(N)\begin{pmatrix}\boldsymbol{\varphi}_{qm}^{\mathrm{TE}}\\ \boldsymbol{\psi}_{qm}^{\mathrm{TE}}\end{pmatrix}(P) + \sum_{m=-N}^{N} U_{qm}^{\mathrm{TM}}(N)\begin{pmatrix}\boldsymbol{\varphi}_{qm}^{\mathrm{TM}}\\ \boldsymbol{\psi}_{qm}^{\mathrm{TM}}\end{pmatrix}(P) \tag{22}$$

where N is the truncation number, and the plus and minus signs represent the direction of propagation. Symbols U_{qm}^{TE} and U_{qm}^{TM} are unknown modal coefficients of the mth order TE and TM modes. It should be noted that the TE- and TM-components should be included in each solution and that the approximations for the electric and magnetic fields have common modal coefficients.

We define the efficiency of the zeroth-order diffracted mode in V_1 as per period power carried away by the zeroth mode normalized by the per period incident power:

$$\rho_0 = \rho_0^{\mathrm{TE}} + \rho_0^{\mathrm{TM}} \tag{23}$$

where the efficiency of the zeroth-order TE and TM mode is given by

$$\rho_0^{\mathrm{TE}} = \frac{\gamma_{10}}{\gamma} \left| U_{10}^{\mathrm{TE}}(N) \right|^2, \quad \rho_0^{\mathrm{TM}} = \frac{\gamma_{10}}{\gamma} \left| U_{10}^{\mathrm{TM}}(N) \right|^2 \tag{24}$$

3. AZIMUTH ANGLE DETECTION

In this section, we introduce the method of azimuth angle detection to improve the resolution of liquid refractive index measurement and the instructions for experiment preparation.

3.1. Method of Azimuth Angle Detection

Conventionally, the excitation of surface plasmon on a metallic grating could be observed by varying the polar angle, accompanied by absorption of the incident TM-wave [16–18]. The absorption occurs at the resonance angle which is sensitive to the refractive index on the surface of the grating [12, 13].

In our new setup, we propose a slight modification to the conventional setup by varying azimuth angle ϕ instead of polar angle θ. Absorption of the incident TM-wave is also observed while varying the azimuth angle ϕ. When a TM wave is incident on a metal grating, enhanced TM-TE mode conversion occurs at angles of incidence at which the surface plasmons are excited [19, 20]. TM-TE mode conversion is observed at a certain azimuth angle ϕ_{sp} at which the surface plasmon is excited, and the resonance angle ϕ_{sp} is also sensitive to the refractive index coated. The enhanced TM-TE mode conversion can be used in precise measurement of the resonance angle. For this purpose, we define the ratio of TE- and TM-components $\rho_0^{\mathrm{TE}}/\rho_0^{\mathrm{TM}}$, where ρ_0^{TE} and ρ_0^{TM} are the efficiencies of the zeroth-order TE- and TM-components, respectively. This phenomenal is similar to varying the polar angle θ; however, the sensitivity could be greatly improved.

3.2. Experimental Details

As shown in Fig. 2, a commercial UV grating (1800GPM, Holographic, Edmund Optics) made of Al with a thin oxide film over-coating is mounted on a stage that rotates about the Z-axis to scan the azimuth angle ϕ with 0.2° steps. The incident light is set on a rotating arm that allows polar angle θ

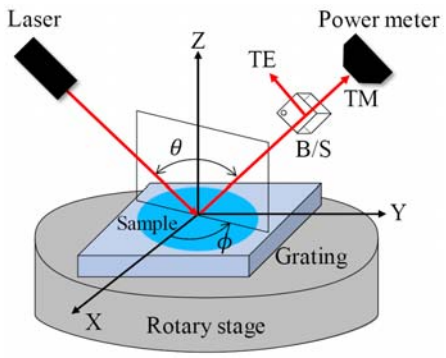

Figure 2. The experimental setup.

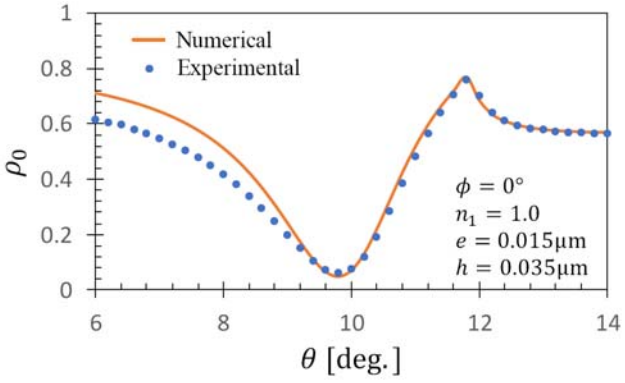

Figure 3. Typical absorption in planar mounting ($\phi = 0°$).

scan with 0.2° steps. The TE- or TM-component of the zeroth diffracted wave is monitored by a power meter through a beam splitter (B/S).

In the following examples, we employ a grating made of aluminum whose parameters are $h = 0.035\,\mu\text{m}$ and $d = 0.556\,\mu\text{m}$. It has a thin oxide film (Al_2O_3, n_2= 1.76, e= 0.015 µm) over-coating. The liquid glycerin is used in the experiment as measurement sample. As an incident light, we choose a TM monochromatic plane wave whose wavelength is λ= 0.670 µm. The refractive index of Al at this wavelength is given by $n_3 = 1.3517 + i7.1150$ [21].

We show typical plasmon resonance absorption in planar mounting ($\phi = 0°$) in Fig. 3. The solid curve and the dots represent numerical result and experimental data. We observe a fairly good agreement between them. The dip in the efficiency at $\theta = 9.8°$ corresponds to the absorption, while the sharp peak at $\theta = 11.8°$ relates to the -1 order cutoff. Note that parameters h and e of the commercial UV grating used in experiment are found through this numerical experiment, which are calculated by mode-matching method [22–25]. The method is a useful technique for computation of boundary-value problems, especially for structures consisting of separate regions. It is based on matching the fields at the boundaries of different regions.

4. PHASE DETECTION

Phase detection is aimed at improving the resolution of the SPR sensor [26–28]. In this section, we explain the rotation analyzer method [29, 30] which can measure the polarization characteristics and phase of diffracted light.

4.1. Polarized Light Analysis

Assuming that the electric field of the diffracted light in the incident region V_1 is $\mathbf{E}_{10}$, its TE and TM components are expressed by Eqs. (25) and (26).

$$\mathbf{E}_{10}^{\text{TE}}(P) = U_{10}^{\text{TE}}(N)\,\boldsymbol{\varphi}_{qm}^{\text{TE}}(P) \tag{25}$$

$$\mathbf{E}_{10}^{\text{TM}}(P) = U_{10}^{\text{TM}}(N)\,\boldsymbol{\varphi}_{qm}^{\text{TM}}(P) \tag{26}$$

Consider a coordinate system consisting of the x axis ($\mathbf{E}_{10}^{\text{TE}}(P)$ direction), y axis ($\mathbf{E}_{10}^{\text{TM}}(P)$ direction), and z axis ($\mathbf{k}_{10}$ direction) with the fractional vector of the diffracted light as $\mathbf{k}_{10}$.

In this coordinate system, the instantaneous values E_x and E_y which are the TE and TM components of the zeroth diffracted electric field are expressed by

$$\mathbf{E}_{10}^{\text{TM}}(P) \to E_x = E_{x0}\cos(\omega t - kz + \delta_x) \tag{27}$$

$$\mathbf{E}_{10}^{\text{TE}}(P) \to E_y = E_{y0}\cos(\omega t - kz + \delta_y) \tag{28}$$

Here, E_{x0} and E_{y0} are the amplitudes of E_x and E_y, and δ_x and δ_y are the initial phases of E_x and E_y, respectively. E_x and E_y in Eqs. (27) and (28) are regarded as electric waves of orthogonal plane waves. The phase difference Δ is given by

$$\Delta = \delta_x - \delta_y \tag{29}$$

The ellipse representing the polarized light of the diffracted light is expressed as:

$$\left(\frac{E_x}{E_{x0}}\right)^2 + \left(\frac{E_y}{E_{y0}}\right)^2 - \frac{2E_x}{E_{x0}}\cdot\frac{E_y}{E_{y0}}\cos\Delta = \sin^2\Delta \tag{30}$$

Figure 4 shows the elliptically polarized light. As shown in Fig. 4, a is the long radius of the ellipse, and b is the short radius. Also, the angle of the amplitude ratio which is the slope from E_y is defined as Ψ. Its tangent is given by

$$\tan\Psi = \frac{E_{x0}}{E_{y0}} \tag{31}$$

A pair of values, Ψ and Δ, are used as parameters representing the polarization of the diffracted light. The coordinate system in Fig. 4 is referred to as a (Ψ, Δ) coordinate system.

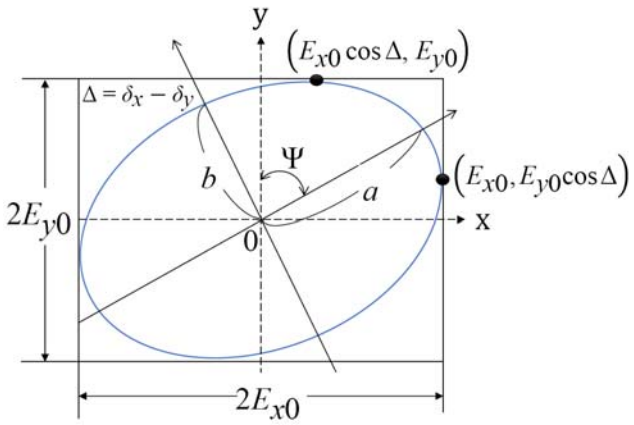

Figure 4. Elliptically polarized light.

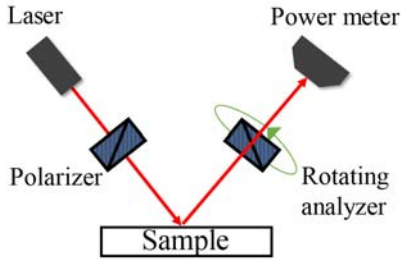

Figure 5. The optical system of rotation analyzer method.

4.2. The Rotation Analyzer Method

The rotation analyzer method is used to measure the polarization state associated with reflection [31, 32]. Fig. 5 shows the optical system of the rotation analyzer method. The rotation analyzer method consists of a laser light source, a polarizer, a sample, a rotating analyzer, and a power meter. The polarizer is inserted perpendicularly to the plane of incidence, and the analyzer is inserted perpendicularly to the plane of reflection. Here, the rotation angle R of the polarizer is set to 45° counterclockwise. After irradiating the sample with the laser, the rotation angle A of the analyzer is rotated clockwise by 5° from 0° to 180°, and the reflected light intensity I is measured with a power meter. I is expressed by Eq. (32) with A as a function

$$I = \frac{I_0}{2}(1+F_1\cos 2A + F_2\sin 2A) \tag{32}$$

I_0 is the average reflected light intensity. Symbols F_1 and F_2 are the normalized Fourier coefficients, which can be determined by Fourier transform. Let $A_l(l = 1, 2, \ldots, n)$ be the rotation angle until the analyzer rotates from 0° to 180°, and let the reflected light intensity corresponding to A_l be I_l. In terms of these values, F_1 and F_2 are computed from

$$F_1 = \frac{\sum_{l=1}^{n}(I_l\cos 2A_l)}{\sum_{l=1}^{n} I_l}, \quad F_2 = \frac{\sum_{l=1}^{n}(I_l\sin 2A_l)}{\sum_{l=1}^{n} I_l} \tag{33}$$

When the rotation angle $R = 45°$, Ψ and Δ can be obtained by

$$\Psi = \tan^{-1}\sqrt{\frac{1+F_1}{1-F_1}}, \quad \Delta = \cos^{-1}\frac{F_2}{\sqrt{1-F_1^2}} \tag{34}$$

The optical system is fixed at a specific polar angle, azimuth angle, and refractive index n_1 of the sample. As a result, Ψ and Δ which change are obtained from Eq. (34).

5. RESULTS AND DISCUSSION

In this section, we consider the surface plasmon resonance absorption of the liquid glycerin refractive index separately for polar angle, azimuth angle, and phase difference detection. We also examine its application as a high-resolution refractive index sensor.

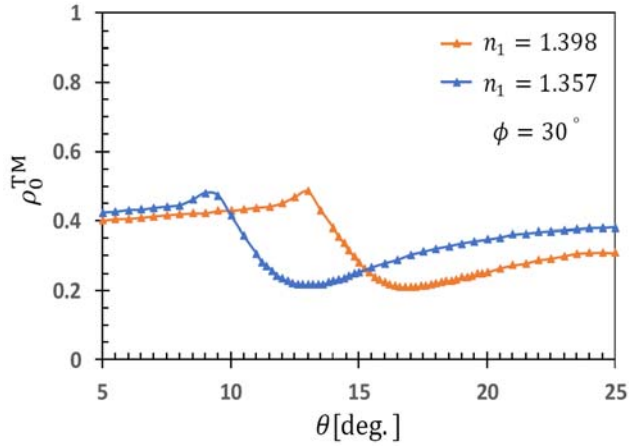

Figure 6. Efficiency of TM-component ρ_0^{TM} according to the polar angle θ.

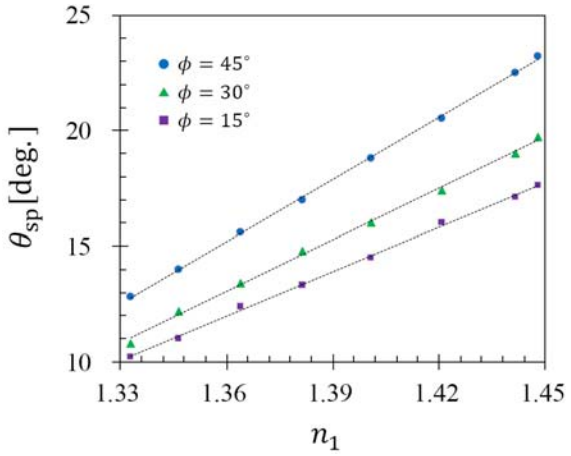

Figure 7. The resonance angle θ_{sp} as a function of refractive index n_1.

5.1. Polar Angle Detection

As a conventional setup result, Fig. 6 shows the efficiency of TM component as a function of the polar angle θ for different refractive indices. We observe that the change of sample refractive index from 1.357 to 1.398 is therefore detected as a shift of a resonance angle θ from 12.8° to 16.8°. As illustrated in Fig. 6, it will be difficult to find the resonance angle due to the "flat-dip effect" of the efficiency which would require a high resolution of the power meter to distinguish different resonance angles close to each other.

Figure 7 shows the resonance angle θ as a function of refractive index. A linear relationship is observed between the absorption angle θ_{sp} and the refractive index for several azimuth angles $\phi = 15°$, 30°, 45°, respectively. As a conventional SPR sensor, the refractive index of the sample is determined by the absorption angle. Further, the resolution is maximized when the azimuth angle is fixed at 45°, and we can achieve a 119°/RIU resolution.

5.2. Azimuth Angle Detection

Figure 8 illustrates ρ_0^{TE}/ρ_0^{TM} as a function of the azimuth angle ϕ for different refractive indices. We observe that the peak shifts from 41° to 26° corresponding to the refractive index changed from 1.357

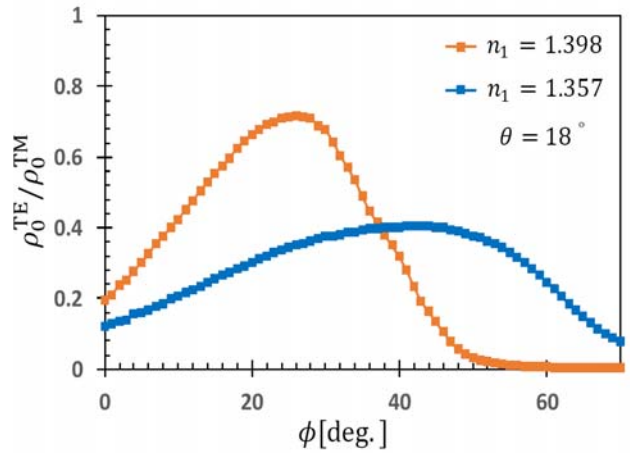

Figure 8. Ratio of TE- and TM-component. ρ_0^{TE}/ρ_0^{TM} according to the azimuth angle ϕ.

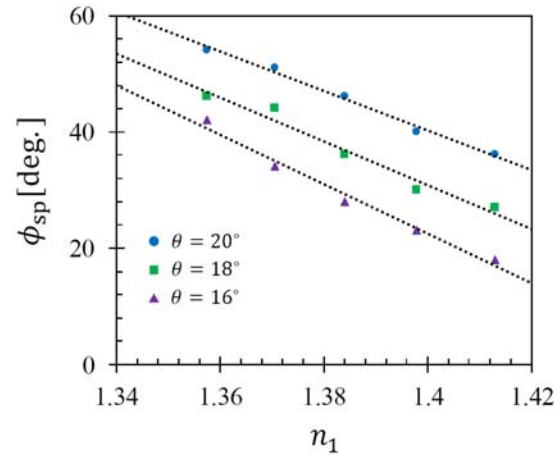

Figure 9. The resonance angle ϕ_{sp} as a function of refractive index n_1.

to 1.398.

Figure 9 shows the resonance angle ϕ as a function of refractive index. In Fig. 9, we observe a negative linear relationship between the absorption angle ϕ_{sp} and refractive index. The resolution is the highest at a polar angle of 16°, and we can realize a 432°/RIU. The resolution is related to the threshold of both the angular and power detections.

5.3. Phase Difference Detection

Figure 10 shows the light intensity I with respect to the rotation angle A of the analyzer. In this case, the incident and azimuth angles are fixed at 13° and 30°, respectively. According to Fig. 10, when n_1 changes, a change in angle of the analyzer having the largest light absorption is observed, indicating that the polarization state of the reflected light is changing.

Figure 11 shows the phase difference Δ of index of the refractive index in glycerin. According to Fig. 11, a linear relationship can be confirmed between n_1 and Δ. The resolution is 1200°/RIU, which is 10 times higher than the polar angle characteristic. If we can measure Δ with two digits after the decimal point, the liquid refractive index can be measured up to five decimal places.

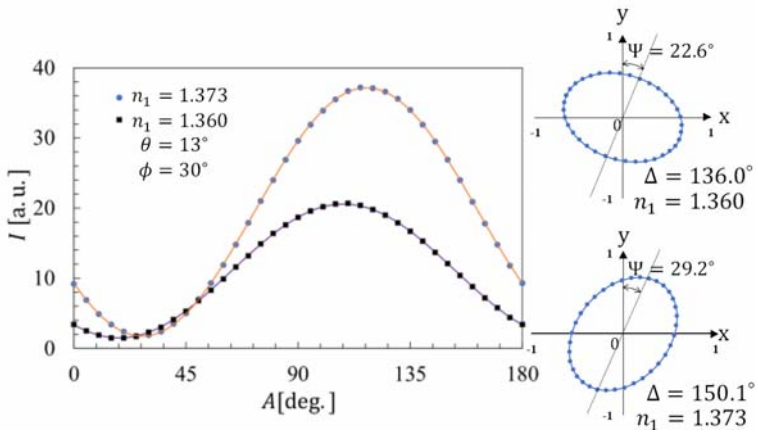

Figure 10. Light intensity of analyzer angles.

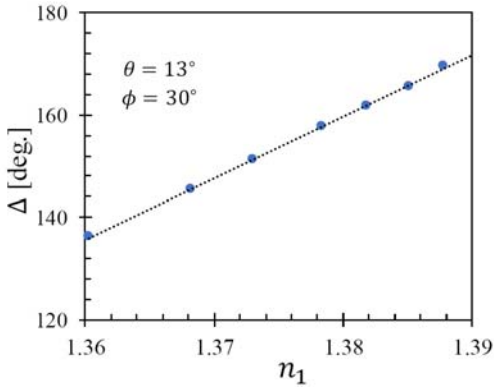

Figure 11. Phase difference Δ as a function of refractive index n_1.

5.4. Comparison of Resolution

In Table 1, we summarize the refractive index resolution by different metrics of polar angle θ, azimuth angle ϕ, and phase difference Δ. The resolution of polar angle detection is 119°/RIU at $\phi = 45°$; the resolution of azimuth angle detection is 432°/RIU at $\theta = 16°$; the resolution is about 3.5 times higher than that of polar angle detection. In the case of phase difference detection, we can realize a 1200°/RIU

Table 1. Comparison of resolution.

Metrics	Setting [deg.]	Resolution [deg./RIU]
Polar angle θ	$\phi = 0$	87
	$\phi = 30$	101
	$\phi = 45$	119
Azimuth angle ϕ	$\theta = 16$	432
	$\theta = 18$	375
	$\theta = 20$	340
Phase difference Δ	$\theta = 13$, $\phi = 30$	1200

by adopting the appropriate polar angle θ and azimuth angle ϕ, and the resolution is 10 times more sensitive than that of the polar angle. We will continue to investigate the physical theory of phase detection in our future research.

6. CONCLUSION

We propose a new setup for SPR sensing applications based on metallic gratings to improve the resolution of an index sensor. We have confirmed that the sensitivity will be greatly improved compared to that of a conventional setup SPR sensor. The resolution of azimuth angle detection is 432°/RIU. Since the sample index has large influence on the phase modulation, the phase detection is a better way to find the index. The resolution of phase detection is 1200°/RIU, which is 10 times more sensitive than that of a conventional setup.

REFERENCES

1. Nevier, M., "The homogenous problem," *Electromagnetic Theory of Gratings*, 123–157, 1980.
2. Raeter, H., "Surface plasmon and roughness," *Surface Polaritons*, 331–403, 1982.
3. Barnes, W. L., T. W. Preist, S. C. Kitson, J. R. Sambles, N. P. K. Cotter, and D. J. Nash, "Photonic gaps in the dispersion of surface plasmons on gratings," *Phys. Rev. B*, Vol. 51, 11164–11167, 1995.
4. Liu, L., L. Ran, H. Guo, X. Chen, and Z. Li, "Broadband plasmonic circuitry enabled by channel domino spoof plasmons," *Progress In Electromagnetics Research*, Vol. 164, 109–118, 2019.
5. Gifford, J. W. and T.M. Lowry, "Some refractive indices of benzene and cyclohexane," *Proc. of the Royal Society of London*, Series A, Vol. 104, No. 726, 430–437, 1923.
6. Thormahlen, I., J. Straub, and U. Grigull, "Refractive index of water and its dependence of wavelength, temperature, and density," *J. Phys. Chem. Ref. Data*, Vol. 14, No. 4, 1985.
7. Cheng, X. and B. Guan, "Optical biosensing and bioimaging with porous silicon and silicon quantum dots (Invited Review)," *Progress In Electromagnetics Research*, Vol. 160, 103–121, 2017.
8. He, S. and H. Dong, "Simultaneous estimation of the refractive index and thickness of marine oil slick from the degree of linear polarization of the sun-glint reflection," *Progress In Electromagnetics Research*, Vol. 163, 133–142, 2018.
9. Rossi, S., E. Gazzola, P. Capaldo, G. Borile, and F. Romanato, "Grating-coupled surface plasmon resonance (GC-SPR) optimization for phase-interrogation biosensing in a microfluidic chamber," *Sensors (Basel)*, Vol. 18, No. 5, 1621, 2018.
10. Lu, H., Y. C. Fan, S. Q. Dai, D. Mao, F. J. Xiao, P. Li, and J. L. Zhao, "Coupling-induced spectral splitting for plasmonic sensing with ultra-high figure of merit," *Chinese Physics B*, Vol. 27, 117302, 2018.
11. Lu, H., S. Dai, Z. Yue, Y. Fan, H. Cheng, J. Di, D. Mao, E. Li, T. Mei, and J. Zhao, "Sb_2Te_3 topological insulator: Surface plasmon resonance and application in refractive index monitoring," *Nanoscale*, Vol. 11, 4759–4766, 2019.
12. Okuno, Y., T. Suyama, and T. Matsuda, "Plasmon resonance-absorption in a dielectric coated metal grating," *IEICE Trans. Electron.*, Vol. J88-C, No. 7, 582584, 2005 (in Japanese).
13. Okuno, Y., T. Suyama, R. Hu, S. He, and T. Matsuda, "Excitation of surface plasmons on a metal grating and its application to an index sensor," *IEICE Trans. Electron.*, Vol. E90-C, No. 7, 1507–1514, 2007.
14. Homola, J., S. Yee, and G. Gauglitz, "Surface plasmon resonance sensors: Review," *Sensors and Actuators B*, Vol. 54, 3–15, 1999.
15. Homola, J., I. Koudela, and S. Yee, "Surface plasmon resonance sensors based on diffraction gratings and prism couplers: Sensitivity comparison," *Sensors and Actuators B*, Vol. 54, 16–24, 1999.
16. Bryan-Brown, G. P., S. J. Elston, and J. R. Sambles, "Coupled surface plasmons on silver coated gratings," *Opt. Commun.*, Vol. 82, 1–5, 1991.

17. Matsuda, T., D. Zhou, and Y. Okuno, "Numerical analysis of plasmon resonance absorption in bisinusoidal metal gratings," *Journal of the Optical Society of America A*, Vol. 19, No. 4, 695–701, 2002.
18. Okuno, Y. and T. Suyama, "Numerical analysis of surface plasmons excited on a thin metal grating," *Journal of Zhejiang University SCIENCE A*, Vol. 7, No. 1, 55–70, 2006.
19. Bryan-Brown, G. P., J. R. Sambles, and M. C. Hutley, "Polarization conversion through the excitation of surface plasmons on a metallic grating," *J. Modern Optics*, Vol. 37, No. 7, 1227–1232, 1990.
20. Matsuda, T., D. Zhou, and Y. Okuno, "Numerical analysis of TE-TM mode conversion in a metal grating placed in conical mounting," *IEICE Trans. Electron.*, Vol. J82-C-I, No. 2, 42–49, 1999.
21. Hass, G. and L. Hadley, "Optical properties of metals," *American Institute of Physics Handbook*, 6–107, 1963.
22. Yasuura, K. and T. Itakura, "Approximation method for wave functions (I), (II), and (III)," *Kyushu Univ. Tech. Rep.*, Vol. 39, No. 1, 51–56, 1966.
23. Yasuura, K., "A view of numerical methods in diffraction problems," *Progress in Radio Science*, 257–270, 1971.
24. Ikuno, H. and K. Yasuura, "Improved point-matching method with application to scattering from a periodic surface," *IEEE Trams. Antennas & Propag.*, Vol. 21, 657–662, 1973.
25. Lawson, C. L. and R. J. Hanson, *Solving Least-Squares Problems*, Prentice-Hall, Englewood Cliffs, NJ, 1974.
26. Nelson, S. G., K. S. Johnston, and S. S. Yee, "High sensitivity surface plasmon resonance sensor based on phase detection," *Sensors and Actuators B*, Vol. 35, Nos. 1–3, 187–191, 1996.
27. Law, W. C., P. Markowicz, K. T. Yong, I. Roy, A. Baev, S. Patskovsky, A. V. Kabashin, H. P. Ho, and P. N. Prasad, "Wide dynamic range phase-sensitive surface plasmon resonance biosensor based on measuring the modulation harmonics," *Biosens. Bioelectron*, Vol. 23, No. 5, 627–632, 2007.
28. Luo, Z., T. Suyama, X. Xu, and Y. Okuno, "A grating-based plasmon biosensor with high resolution," *Progress In Electromagnetics Research*, Vol. 118, 527–539, 2011.
29. Budde, W.,"Photoelectric analysis of polarized light," *Opt.*, Vol. 1, 201–205, April 1962.
30. Horowitz, P. and W. Hill, *The Art of Electronics*, 641–646, Cambridge University Press, Cambridge, 1989.
31. Matsuda, T. and S. Hayashi, "Polarization of diffracted wave form periodic structures in resonance region," *IEEJ*, Vol. EMT-06-106, 115–119, 2006.
32. Lin, B. Q., J. Guo, Y. Wang, Z. Wang, B. Huang, and X. Liu, "A wide-angle and wide-band circular polarizer using a BI-Layer metasurface," *Progress In Electromagnetics Research*, Vol. 161, 125–133, 2018.